frontiers | Frontiers in Materials

ORIGINAL RESEARCH
published: 08 June 2022
doi: 10.3389/fmats.2022.908789

Nano-Sonosensitized Sonodynamic Nanomedicine Augments Tumor-Selective Catalytic Tumor Eradication

Haixian Zhang[†,1], *Yiming Li*[†,2], *Junying Liu*[1] *and Cai Chang*[1]*

[1]Department of Ultrasound, Fudan University Shanghai Cancer Center, Department of Oncology, Shanghai Medical College, Fudan University, Shanghai, China, [2]Department of Ultrasound, Huashan Hospital, Fudan University, Shanghai, China

Inspired by the distinct metabolic pathway of tumor cells, here a new anti-cancer therapy (i.e., Cu-TCPP(Fe) metal-organic frameworks (MOFs) with sonosensitizer for sonodynamic therapy (SDT) and tumor microenvironment (TME)-specific release of copper/iron for chemical catalysis) is introduced and verified. Upon exposure to ultrasound, the porphyrin structure in the MOFs yields reactive oxygen species (ROS), and the copper/iron induces the Fenton reaction in the TME existing H_2O_2 and acid. Thus, highly toxic ROS are generated through these TME-specific reactions to trigger the apoptosis and death of tumor cells. The current work paves a new avenue to design SDT with catalytic nanomedicine for the selective and effective treatment of tumors.

Keywords: metal-organic frameworks, Cu-TCPP(Fe), sonodynamic therapy, Fenton reaction, catalytic

OPEN ACCESS

Edited by:
Mingqiang Li,
Third Affiliated Hospital of Sun Yat-sen University, China

Reviewed by:
Wei Feng,
Shanghai University, China
冉 海涛,
Chongqing Medical University, China

***Correspondence:**
Cai Chang
changc61@163.com

†These authors have contributed equally to this work

Specialty section:
This article was submitted to Biomaterials, a section of the journal Frontiers in Materials

Received: *31 March 2022*
Accepted: *26 May 2022*
Published: *08 June 2022*

Citation:
Zhang H, Li Y, Liu J and Chang C (2022) Nano-Sonosensitized Sonodynamic Nanomedicine Augments Tumor-Selective Catalytic Tumor Eradication. Front. Mater. 9:908789. doi: 10.3389/fmats.2022.908789

1 INTRODUCTION

Malignant tumors are a global public health issue (Siegel et al., 2021). Although striking progress has been made in the area of targeted cancer therapy, the anticancer effect of molecular targeted treatment is still inadequate (Cheng et al., 2014; Chu and Dupuy, 2014; Liu et al., 2015a; Zhang et al., 2015; Long et al., 2016; Pelaz et al., 2017). To better understand the tumor microenvironment (TME), tumor cellular metabolism, biosynthetic intermediates, and the physical environment have been broadly studied (Carmeliet and Jain, 2000; Coussens and Werb, 2002; Hanahan and Weinberg, 2011; Wang et al., 2017). Among all TME signals, reactive oxygen species (ROS) (Trachootham et al., 2009; DeBerardinis and Chandel, 2016; Hornsveld and Dansen, 2016)—chemically reactive molecules containing oxygen, including hydroxyl radical (•OH), superoxide anion (O_2•-), singlet oxygen ($^1O_2$), and hydrogen peroxide (H_2O_2)—were found to be important messengers in the cell. Changes in the levels of ROS influence cell proliferation, differentiation, apoptosis, or necrosis. Low levels of ROS promote cell proliferation and survival. However, excess production of ROS can induce cell senescence and death by causing oxidative damage to intracellular biomacromolecules, such as proteins, lipids, RNA, and DNA (Landry and Cotter, 2014; Galadari et al., 2017; Zou et al., 2017). Therefore, ROS-mediated cancer therapy has gained increasing attention (Dolmans et al., 2003; Castano et al., 2006; Allison and Sibata, 2010; Firczuk et al., 2011). It should be noted that increasing ROS levels via molecular-targeted drugs is a novel therapeutic regimen for treating cancer patients with drug-resistant tumors.

As an emerging non-invasive management technique for malignant tumors, sonodynamic therapy (SDT) has received extensive attention in recent years (Deepagan et al., 2016; McEwan et al., 2016; Huang et al., 2017a; Kou et al., 2017). Similar to photodynamic therapy, SDT uses

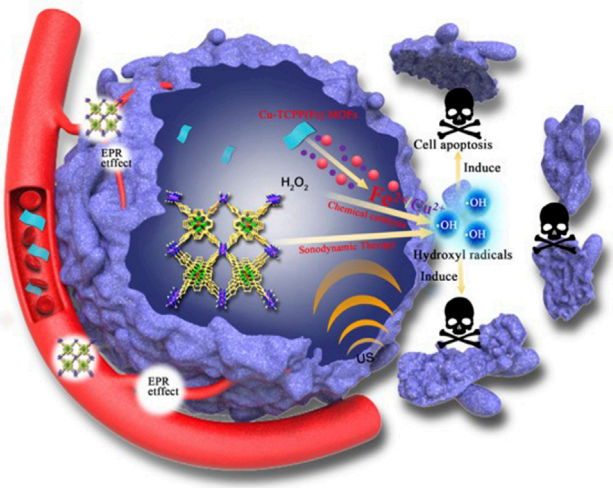

FIGURE 1 | Schematic illustration of the synergistic SDT/chemical catalytic-therapeutic mechanism of Cu-TCPP(Fe) MOFs against cancer.

therapeutic ultrasound (US) waves to activate a sonosensitizer (e.g., porphyrins) to generate ROS, which directly induces cancer cell death (Harada et al., 2011; Li et al., 2016). Moreover, SDT has been considered as a potential complementary treatment to conventional cancer chemotherapy because of its deep-tissue penetration, high spatial accuracy, and biosafety features. Additionally, advancements in novel nanomaterials have enhanced the accuracy of SDT and mitigated its side effects. Metal-organic frameworks (MOFs) have been receiving substantial consideration for various applications due to their tunable structure and function, large surface area, and highly ordered pores for substrate molecules (Strickland et al., 2015; Huang et al., 2017b; Guo et al., 2017; Simon-Yarza et al., 2017).

It is plausible that approaches that increase production ROS in a controlled manner may serve as alternative strategies to SDT. For example, the Fenton reaction has been used for the production of •OH—one of the strongest oxidants in nature (Burkitt and Gilbert, 1990; Portnow et al., 2009; Rahim Pouran et al., 2014; Hofmans et al., 2016). Therefore, in this work (**Figure 1**), we report a sonodynamic agent based on MOFs that possess enhanced sonodynamic effects in combination with the Fenton reaction, which highlights the potential clinical application of SDT combined with chemical catalysis in anti-cancer management.

2 RESULTS AND DISCUSSION

2.1 Design, Synthesis, and Characterization of Cu-TCPP(Fe)

The application of MOFs, a new type of 2-dimensional (2D) nanomaterial with unique physical and chemical properties (Novoselov et al., 2004; Chhowalla et al., 2013; Pakdel et al., 2014; Ma and Sasaki, 2015; Tan and Zhang, 2015; Liu et al., 2016; Huang et al., 2017b), has been widely explored in many fields, such as hydrogen storage and theranostic nanomedicine (Peng et al., 2014; Rodenas et al., 2015). In this work, water-stable, 2D, metalloporphyrinic MOFs, labeled as Cu-TCPP(Fe), were fabricated by TCPP(Fe) [TCPP = tetrakis (4-carboxyphenyl) porphyrin] as ligands and $Cu_2(COO)_4$ paddle-wheel clusters as metal nodes. The four $Cu_2(COO)_4$ paddle-wheels were used as the linkage of the 2D "checkboard" motif of TCPP(Fe) for each layered sheet, and the layered sheets were stacked in an AB-packing pattern (**Figure 2A**). The as-prepared Cu-TCPP(Fe) MOFs were dispersed in water for several weeks in a tightly sealed bottle. Digital photographs of Cu-TCPP(Fe) MOFs dispersed in water with typical Tyndall effects indicated their excellent hydrophilicity and dispersity (**Figure 2B**). Transmission electron microscopy (TEM) image showed low contrast of the obtained nanosheets with sizes ranging from hundreds of nanometers to a few micrometers (**Figure 2C**), confirming the ultrathin nature of the Cu-TCPP(Fe) MOFs. The TEM images also displayed typical Cu-TCPP(Fe) MOFs (**Figure 2D**). The corresponding selected area electron diffraction (SAED) pattern (**Figure 2E**) also confirmed the basal plane's hexagonal symmetry structure, demonstrating its highly crystallized structure. The quantitative element analysis was determined by the inductively-coupled plasma optical emission spectroscopy (ICP-OES) (Cu: Fe = 2:1). X-ray diffraction (XRD) patterns exhibited characteristic diffraction peaks of 8.8°, 10.6°, and 19.2°, which were assigned to (110), (001), and (002) (Makiura et al., 2010; Xu et al., 2012), further verifying the crystalline nature of the 2D Cu-TCPP(Fe) nanosheets (**Figure 2F**). X-ray photoelectron spectroscopy (XPS) analysis was carried out to verify the oxidation states of copper/iron in the Cu-TCPP(Fe) nanosheet. The XPS peaks for the Cu-TCPP(Fe) MOFs showed Fe^{II} and its satellite peaks at 707.23 eV and 718.44 eV, and the Fe^{III} peaks at 711.51 eV and 725.76 eV, demonstrating the coexistence of Fe^{II} and Fe^{III} in the MOFs (**Figure 2G**). Deconvolution of the MOFs signal was used to determine the portion of Fe^{II} (59.55% and 12.34%) and Fe^{III} (23.76% and 4.35%) in the sample.

To enhance the stability of the Cu-TCPP(Fe) nanosheets in the physiological environment of the human body and lengthen the internal circulation time, their surface was grafted with a biocompatible soybean phospholipid (SP). These surface-modified Cu-TCPP(Fe) nanosheets featured high colloidal stability in physiological solutions, such as Dulbecco's modified Eagle's medium (DMEM) and phosphate buffer saline (PBS).

2.2 *In vitro* Reactive Oxygen Species Generation and Cytotoxicity by Fenton Reaction

We used 3,3′,5,5′-tetramethylbenzidine (TMB), a widely-used substrate for the assay of enzyme mimic catalytic performance (Gao et al., 2007; Chen et al., 2012; Su et al., 2012; An et al., 2013; Liu et al., 2015b; Kwon et al., 2016; Zhang et al., 2016), to assess the peroxidase-like catalytic activity of Cu-TCPP(Fe) and the enhancement of SDT (**Figure 3A**). The Cu/Fe in Cu-TCPP(Fe)

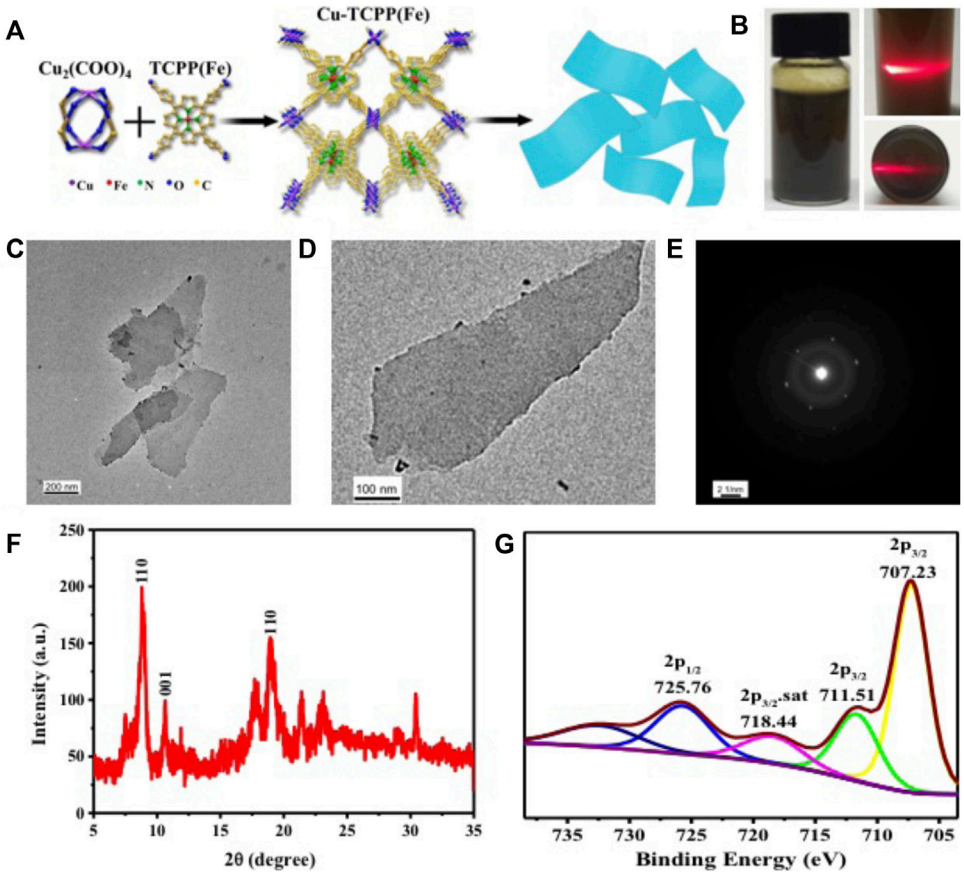

FIGURE 2 | Characterization of Cu-TCPP(Fe) MOFs. **(A)** A schematic showing the synthetic procedure for Cu-TCPP(Fe) MOFs. **(B)** A digital photograph and **(C)** TEM image of Cu-TCPP(Fe) MOFs. **(D)** A TEM image and **(E)** SAED pattern of a typical Cu-TCPP(Fe) MOF. **(F)** XRD patterns, and **(G)** XPS spectra of Cu-TCPP(Fe) MOFs.

initially catalyzed H_2O_2 to produce highly toxic hydroxyl radicals (•OH) in the acidic environment (**Equation 1**), which then oxidized the colorless TMB to form chromogenic oxidized TMB (ox-TMB) with a λ_{max} = 650 nm. The catalytic functionalities and performances of Cu-TCPP(Fe) were explored by plotting typical Michaelis-Menten steady-state kinetics. H_2O_2 (40, 20, 10, and 5 mM) served as the reactants in the assays of 20 μg/ml Cu-TCPP(Fe) and the trigger of US (1.0 MHz, 1.5 W/cm^2, 50% duty cycle, 1 min) implied that SDT could enhance enzyme mimic catalytic performance (**Figure 3B**). The time-course absorbance upon the addition of H_2O_2 into the Cu-TCPP(Fe) in sodium citrate buffer solution (pH = 6.0) was plotted, and the corresponding average initial velocities were calculated. Michaelis-Menten steady-state kinetics of Cu-TCPP(Fe) was plotted (**Equation 2**). All average initial velocities of absorbance changes were then converted as initial velocities (v_0) of cation-free radical production or hydroxyl radical formation *via* the Beer-Lambert law (**Equation 3**), and then plotted against the corresponding concentration and fitted with Michaelis-Menten curves (**Figure 3D**). The ox-TMB resulted in the blue color in the solutions (inset in **Figure 3C**), which showed a maximum absorption peak at 650 nm (**Figure 3C**), demonstrating that the cascade reaction occurred. A linear double-reciprocal plot (Lineweaver-Burk plot, **Equation 4** and **Figure 3E**) was obtained to determine the Michaelis-Menten constant (K_M) and maximum velocity (V_{max}). The K_M and V_{max} values were calculated to be 33.60 mM and 1.2 × 10^{-3} M/s for Cu-TCPP(Fe).

$$H_2O_2 + Cu^{2+}/Fe^{2+} = Cu^{2+}/Fe^{3+} + \bullet OH + OH^- \quad (1)$$

$$A = kbc \quad (2)$$

$$v_0 = \frac{V_{max} \cdot [S]}{K_M + [S]} \quad (3)$$

$$\frac{1}{v_0} = \frac{K_M}{V_{max}} \cdot \frac{1}{[S]} + \frac{1}{V_{max}} \quad (4)$$

The methylene blue (MB) dye test (**Figure 5A**) was performed to determine the presence of hydroxyl radicals generated by the Fenton reaction (Satoh et al., 2007; Zhang et al., 2015). •OH radicals are the primary active substances for MB bleaching in the traditional Fe^{2+}/H_2O_2 system. Importantly, the added H_2O_2 did not cause obvious MB bleaching (**Figure 4C**) as compared to the MB group (**Figure 4B**), whereas the MB with the H_2O_2 group was homogeneously dark blue. The introduction of Cu-TCPP(Fe) cause obvious MB bleaching (**Figure 4D**) and adding US (1.0 MHz, 1.5 W/

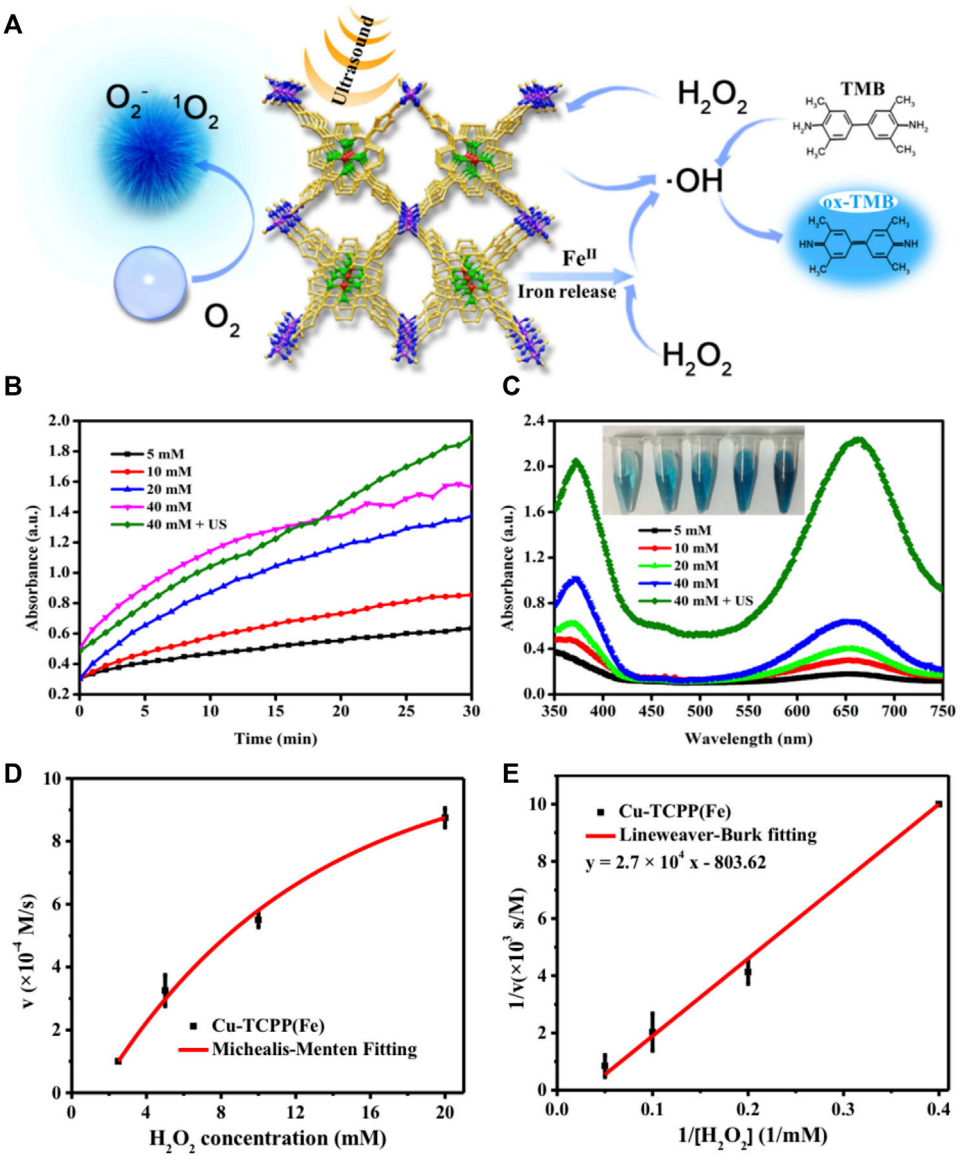

FIGURE 3 | *In vitro* characterizations of the catalytic performance of Cu-TCPP(Fe). **(A)** Schematic illustration of the mechanism of ROS generation by employing Cu-TCPP(Fe) as sonosensitizer for SDT (left) and chemical catalyze (right). **(B)** The absorbance of Cu-TCPP(Fe) over time after the addition of varied concentrations of H_2O_2 (40, 20, 10, and 5 mM) and the trigger of US (1.0 MHz, 1.5 W/cm^2, 50% duty cycle, 1 min) at pH = 6.0, with 0.8 mg/ml TMB and 20 μg/ml Cu-TCPP(Fe). **(C)** Absorbance spectra changes (λ_{max} = 650 nm) at the end of the reaction (inset shows the photographs of ox-TMB). **(D)** Michaelis-Menten kinetics and **(E)** Lineweaver-Burk plotting of Cu-TCPP(Fe).

cm^2, 50% duty cycle, 1 min) implied that SDT could enhance the Fenton reaction (**Figure 4E**). The bleaching of MB in the Cu^{2+}/Fe^{2+}/H_2O_2 system can be divided into two stages: the short initial stage and the long deceleration stage. In the short initial stage, the •OH generation rate was rapid, which led to a rapid drop in MB concentration (**Figure 4F**). However, after H_2O_2 and Cu^{2+}/Fe^{2+} were rapidly consumed during the short initial stage, the bleaching reaction entered the long deceleration stage. The bleaching of MB resulted in the pale blue color in the solutions (inset in **Figure 4F**), which showed a maximum absorption peak at 664 nm.

2.3 Intracellular Biodegradation of Cu-TCPP(Fe)

Bio-TEM was employed to perceive the underlying evolution of Cu-TCPP(Fe) after co-culture with 4T1 cells over time [(Chu and Dupuy, 2014; Liu et al., 2015a; Pelaz et al., 2017; Siegel et al., 2021) d] (**Figure 5A**). The Cu-TCPP(Fe) was endocytosed well after 1 d co-incubation. Subsequently, some nanoparticles were degraded and excreted from the cells. As co-incubation continued, an increasing amount of nanoparticles were degraded and barely any nanoparticles were observed after 7 d.

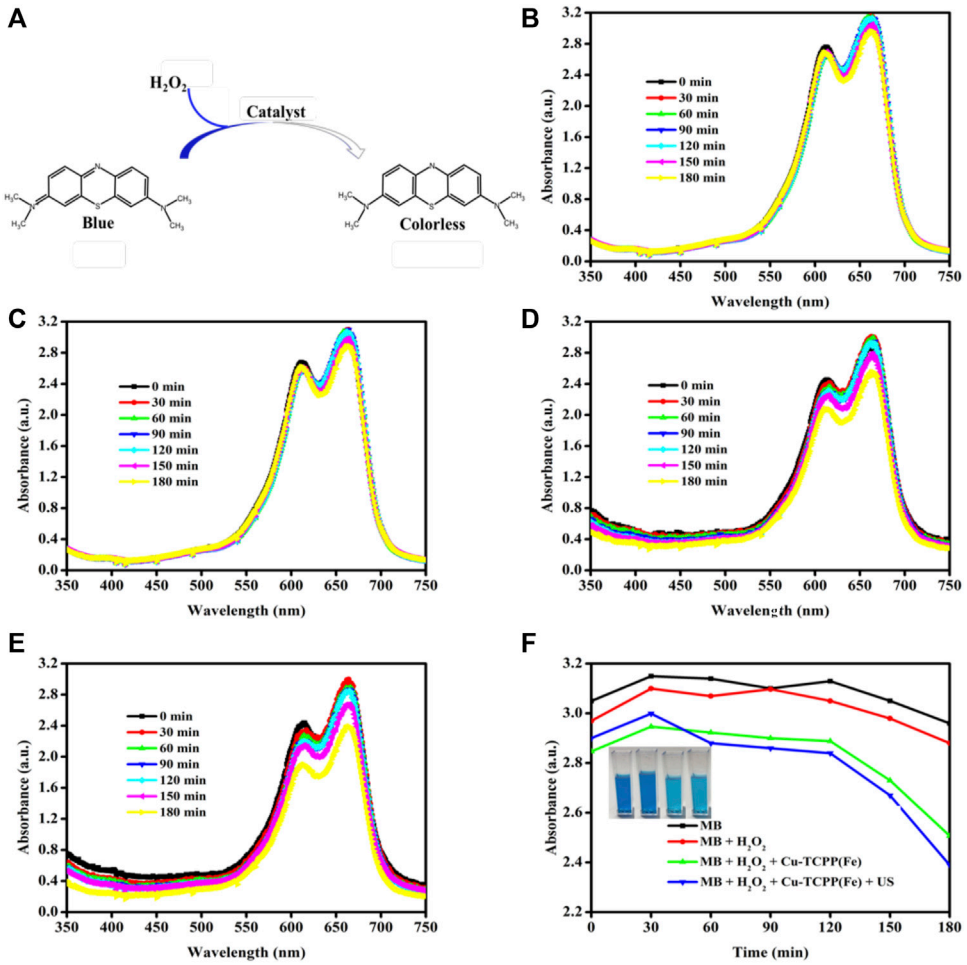

FIGURE 4 | MB bleaching test. **(A)** The sketch map of MB bleaching. MB absorbance spectra changes (λ_{max} = 664 nm) at different time points (0, 30, 60, 90, 120, 150, and 180 min) after initiation of the Fenton reaction at **(B)** pH = 6.0, **(C)** pH = 6.0 + 40 mM H_2O_2, **(D)** pH = 6.0 + 40 mM H_2O_2 + 40 μg/ml Cu-TCPP(Fe) and **(E)** pH = 6.0 + 40 mM H_2O_2 + 40 μg/ml Cu-TCPP(Fe) + US (1.0 MHz, 1.5 W/cm^2, 50% duty cycle, 1 min). **(F)** Comparison of ROS production in different treatments as determined by MB absorption.

2.4 *In vitro* Sonodynamic Therapy/Chemical Catalysis Therapy for Cancer

The above-mentioned *in vitro* research was shown to yield a substantial amount of hydroxyl radicals by Cu-TCPP(Fe). The CCK-8 assay was used to define the inherent toxicity of Cu-TCPP(Fe) by using 4T1 cells. Furthermore, 4T1 cells were initially co-cultured with Cu-TCPP(Fe) at various concentrations (20, 10, 5, 2.5, 1.25, and 0.625 μg/ml) for 12 and 24 h. No obvious cytotoxicity of Cu-TCPP(Fe) nanocomposites was observed (**Figure 5B**). 4T1 cells were then incubated at different pH values (7.0, 6.5, 6.0, 5.5, 5.0, 4.5, 4.0, 3.5, and 3.0) for 12 h. No obvious cytotoxicity was observed at pH values between 5.0–7.0 (**Figure 5C**). To observe the cytotoxicity of the Fenton reaction of Cu-TCPP(Fe), 4T1 cells were then incubated with Cu-TCPP(Fe) at various concentrations (20, 10, 5, 2.5, 1.25, and 0.625 μg/ml) under acidic (pH = 6.0) and neutral (pH = 7.4) culture mediums for 4 h. The Cu-TCPP(Fe) present 47.76, 62.87, 61.46, 70.12, 76.66, 85.94, 91.91, 91.55, 94.94, 95.21, 96.25% cell viabilities at descendent concentrations under the acidic (pH = 6.0) and neutral (pH = 7.4) condition, respectively. This confirmed that the cell viability is dependent upon the quantity of Cu-TCPP(Fe) and the pH value (**Figure 5D**). Concurrently, a CCK-8 assay was also used to define the toxicity of Cu-TCPP(Fe) as a sonosensitizer. Cu-TCPP(Fe) alone exhibits negligible cytotoxicity, whereas Cu-TCPP(Fe) combined with SDT significantly improved the treatment efficiency, inhibited cell proliferation, and induced cell death. These effects were Cu-TCPP(Fe) concentration- and US irradiation time (30, 60, and 120 s)-dependent (**Figure 5E**).

To validate the synergistic effect induced by SDT and the Fenton reaction of Cu-TCPP(Fe), a CCK-8 assay, calcein acetoxymethyl ester (calcein-AM)/propidium iodide (PI) solution stain test, and 2′-7′-dichlorofluorescein diacetate (DCFH-DA) test were conducted. For the CCK-8 assay, 4T1

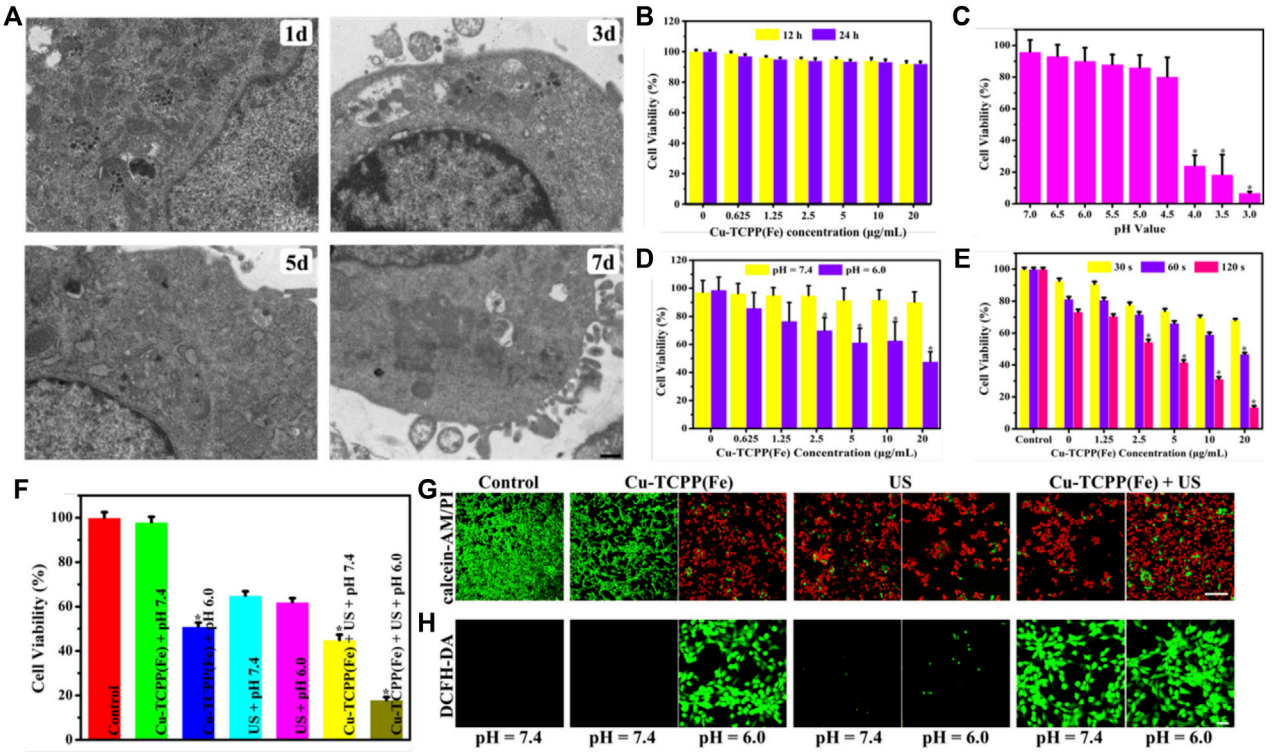

FIGURE 5 | *In vitro* SDT/chemical catalysis therapy for cancer. **(A)** Bio-TEM images for the intracellular biodegradation behavior of Cu-TCPP(Fe) in 4T1 cells after co-incubation over time (Chu and Dupuy, 2014;Liu et al., 2015a; Pelaz et al., 2017; Siegel et al., 2021) **(D)**. **(B)** Viability of 4T1 cells after incubation with various concentrations of Cu-TCPP(Fe) for 12 and 24 h. **(C)** Viability of 4T1 cells after incubation at various pH values (7.0, 6.5, 6.0, 5.5, 5.0, 4.5, 4.0, 3.5 and 3.0) for 12 h. **(D)** Cytotoxicity profiles of 4T1 cells treated with Cu-TCPP(Fe) under neutral (pH = 7.4) and acidic (pH = 6.0) conditions. **(E)** Viability of 4T1 cells after exposure to US irradiation (1.0 MHz, 1.5 W/cm^2, 50% duty cycle) over time (30, 60, and 120 s) at various Cu-TCPP(Fe) concentrations (20, 10, 5, 2.5, 1.25 μg/ml). **(F)** Relative viabilities of 4T1 cells after different treatments, including control (without any treatment), Cu-TCPP(Fe) at pH = 7.4/6.0, US irradiation at pH = 7.4/6.0, and Cu-TCPP(Fe) combined with US irradiation at pH = 7.4/6.0. CLSM images of 4T1 cells stained with calcein AM/PI solution **(G)** and the ROS fluorescent probe DCFH-DA **(H)** after different treatments (scale bar: 50 μm). *$p < 0.05$, calculated by one-way ANOVA test.

cells were incubated with Cu-TCPP(Fe) at 20 μg/ml for 4 h at a pH = 7.4 or pH = 6.0, with or without US (1.0 MHz, 1.5 W/cm^2, 50% duty cycle, 1 min) irradiation. As revealed in **Figure 5F**, the cells were largely eradicated by US irradiation after co-incubation with Cu-TCPP(Fe) under acid conditions (pH = 6.0). The viability of cancer cells by Cu-TCPP(Fe) combined with US irradiation under acidic conditions decreased to nearly 18%, which was much lower as compared to neutral conditions at the same concentration (20 μg/ml) under the same US irradiation conditions. The drastically enhanced sonotoxicity of Cu-TCPP(Fe) under acidic conditions was ascribed to the immense production of ROS enhanced by the Fenton reaction. To visually observe the cells, 4T1 cells were stained with calcein-AM/PI solution after co-culturing with 20 μg/ml Cu-TCPP(Fe) at pH = 7.4 or pH = 6.0 conditions for 4 h. The viable cells emitted green fluorescence, while the dead cells emitted red fluorescence as witnessed by confocal laser scanning microscope (CLSM) (**Figure 5G**). The CLSM showed that the 4T1 cells were impaired at pH = 7.4. A vast amount of dead cells were observed at pH = 6.0. These results were consistent with the cytotoxicity profiles of Cu-TCPP(Fe), which was assumed to be initiated by the toxic hydroxyl radicals produced *in situ* by Cu-TCPP(Fe).

To unveil the intracellular mechanism of Cu-TCPP(Fe) as sonosensitizers that kill tumor cells, DCFH-DA was used to show that the ROS levels within the cell (**Figure 5H**). Cu-TCPP(Fe) + US irradiation (1.0 MHz, 1.5 W/cm^2, 50% duty cycle, 60 s) induced substantial intracellular ROS production, as manifested by the production of considerable green fluorescence in tumor cells. The control, as well as the US and Cu-TCPP(Fe) pH = 7.4 group, displayed a low level of green fluorescence, indicating the increased production of ROS through the sonodynamic method combined with Cu-TCPP(Fe).

2.5 The *in vivo* Synergistic Effects of Sonodynamic Therapy and Chemical Catalysis of Cu-TCPP(Fe)

Encouraged by the excellent synergy of SDT and the chemical catalysis of Cu-TCPP(Fe), the *in vivo* synergistic effects of this combination were further assessed by using intravenous administration of the Cu-TCPP(Fe) into 4T1 tumor-bearing mice followed by various treatments. Several evaluations were carried out to estimate the *in vivo* biocompatibility of Cu-TCPP(Fe) before subsequent *in vivo* therapeutic evaluation.

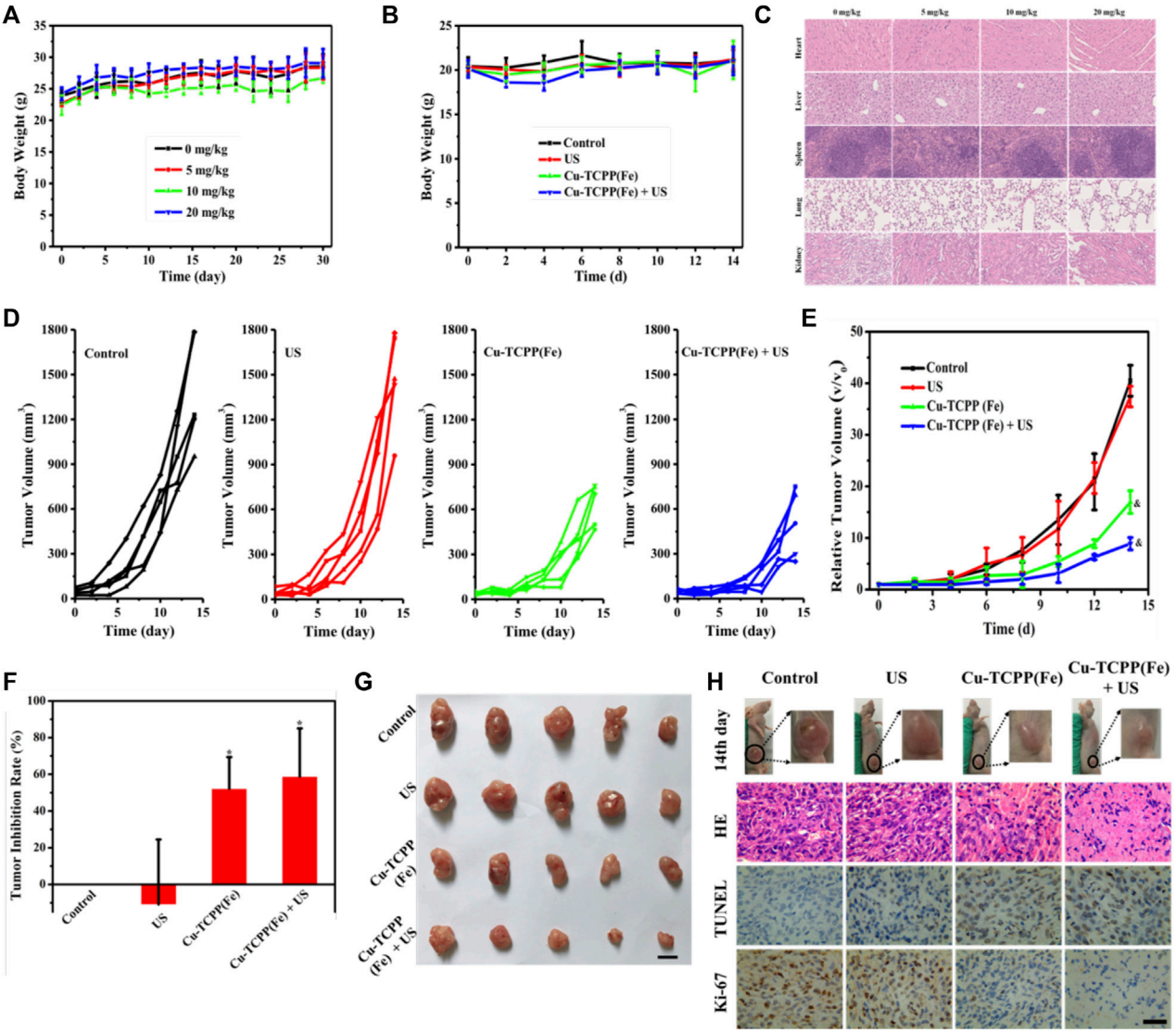

FIGURE 6 | *In vivo* synergistic SDT/chemical catalysis for tumor suppression. **(A)** The bodyweight of mouse changes in the biocompatibility evaluation. **(B)** Bodyweight changes of 4T1 tumor-bearing mice in different groups. **(C)** H&E-stained histological images of organs in the biocompatibility evaluation; scale bar: 50 μm. Time-dependent tumor-growth curves **(D)**, relative tumor volume **(E)**, and tumor inhibition rate **(F)** of 4T1 tumor-bearing mice in four experimental groups (n = 5), including the control group, US group, Cu-TCPP(Fe) group, and Cu-TCPP(Fe) + US group. **(G)** Photographs of the dissected tumors from four groups after 2 weeks of treatment (scale bar: 10 mm). **(H)** H&E staining, TUNEL staining, and Ki-67 immunohistochemical staining of tumor tissue from each group after different treatments (scale bar: 50 μm). &$p < 0.05$, calculated by repeated measure ANOVA test. *$p < 0.05$, calculated by one-way ANOVA test.

Healthy Kunming mice (n = 5) were administrated with Cu-TCPP(Fe) (0, 5, 10, and 20 mg/kg) *via* tail vein injections. No obvious major organ damage was detected one-month post-injection, as confirmed by body weight (**Figure 6A**), hematology (**Figures 7A–D**), serum biochemistry (**Figures 7E,F**), and histological analyses (**Figure 6C**). Then 20 tumor-bearing mice were randomly divided into four groups (n = 5 per group), including the control group (treated with saline), US group, Cu-TCPP(Fe) group, and Cu-TCPP(Fe) + US group. The US irradiation groups were treated with US irradiation on the first and fifth day. The body weight and tumor volume of the four groups were recorded every 2 d (**Figures 6B,D**). The tumor-bearing mice in the control and US group experienced rapid tumor growth, while the tumor growth was significantly inhibited in the Cu-TCPP(Fe) and Cu-TCPP(Fe) + US group, ultimately demonstrating the therapeutic efficacy of SDT and its synergetic effect with the chemical catalysis (**Figure 6E**). The tumor inhibition rate in the Cu-TCPP(Fe) group and Cu-TCPP(Fe) + US group reached 52.2% and 58.8%, respectively (**Figure 6F**). At the end of the therapeutic treatment, the tumors in the mice of all groups were imaged, dissected, and compared (**Figure 6G**). We found that 4T1 tumor growth was effectively inhibited after the intravenous administration of Cu-TCPP(Fe). To further study the synergistic effect of various treatments, H&E, TUNEL, and

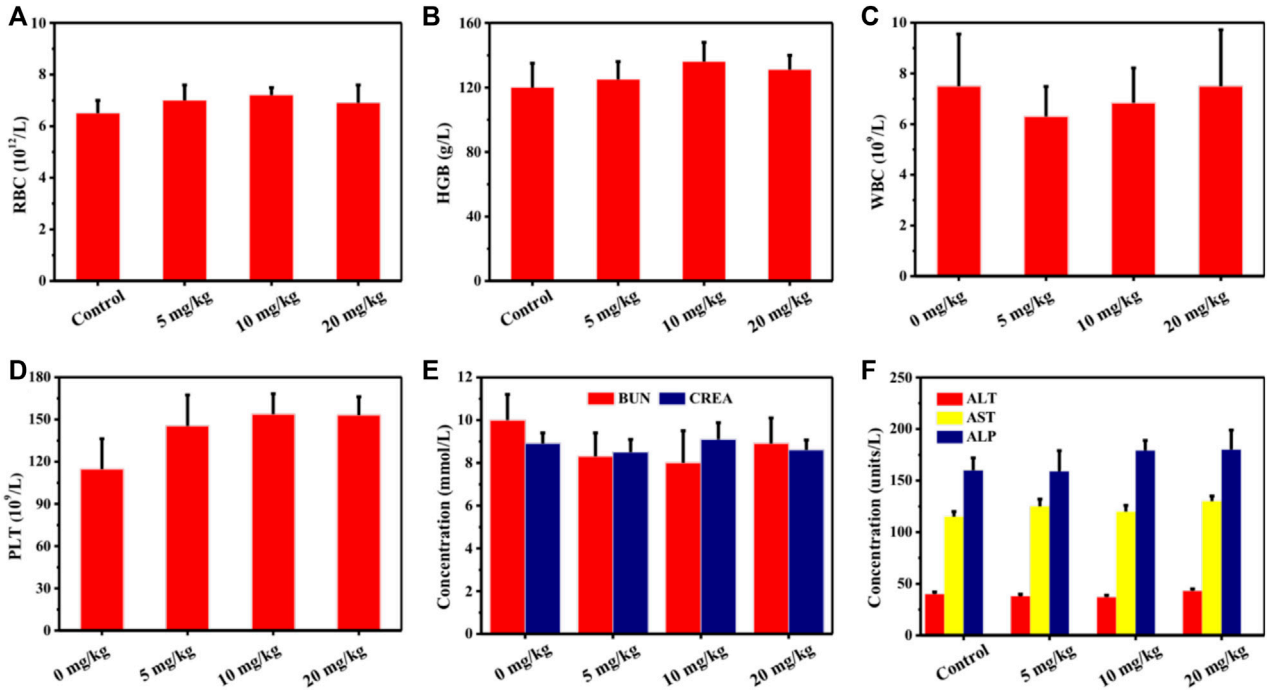

FIGURE 7 | Blood routine examination and serum biochemical levels of mice treated with 0 mg/kg, 5 mg/kg, 10 mg/kg, and 20 mg/kg of Cu-TCPP(Fe). **(A)** Red blood cell (RBC), **(B)** Hemoglobin (HGB), **(C)** White blood cell (WBC), **(D)** Platelet (PLT), **(E)** Blood urea nitrogen (BUN) and creatinine (CREA), **(F)** Alanine transaminase (ALT), aspartate aminotransferase (AST) and alkaline phosphatase (ALP) levels of mice in all groups.

Ki-67 antibody staining were performed on tumor sections from all groups of mice at 24 h post-treatment (**Figure 6H**). Additionally, H&E and TUNEL results showed that a large number of dead cells were observed in the tumor tissue. The Cu-TCPP(Fe) alone and combined with US exhibited greater necrosis and apoptosis rates as compared to the control and US group. The Ki-67 results of each group were in agreement with the H&E and TUNEL staining results, confirming the efficacy of SDT and its synergistic effects with chemical catalysis. Furthermore, there was no noticeable adverse effects or organ damage to the heart, liver, spleen, lung, and kidney in the treatment groups (**Figure 8**).

3 EXPERIMENTAL SECTION

3.1 Materials and Reagents

Copper nitrate trihydrate [$Cu(NO_3)_2{\cdot}3H_2O$, 99%], N,N-dimethylformamide (DMF, 99.8%), hydrogen peroxide (H_2O_2, 30 wt%), soybean phospholipid (SP), and 3,3′,5,5′-tetramethylbenzidine (TMB, 99%) were purchased from Sigma-Aldrich (Shanghai, China). 3,7-bis(dimethylamino)-phenothiazin-5-ium chloride (methylene blue dye, MB, 97%) was purchased from Fluka (Buchs, Switzerland). Fe(III) meso-tetra(4-carboxyphenyl) porphine chloride [TCPP(Fe), 97%] was purchased from J&K Chemical Ltd. (Shanghai, China). Ethanol (99.9%) was purchased from Merck (Nordic European Centre, Singapore). Trifluoroacetic acid (CF_3COOH, 99%) was purchased from Alfa Aesar (Haverhill, Massachusetts, United States). 2′-7′-dichlorofluorescein diacetate (DCFH-DA) was bought from Beyotime Institute of Biotechnology. Calcein acetoxymethyl ester (calcein-AM) and propidium iodide (PI) were purchased from Thermo Fisher Scientific Inc. Dulbecco's Modified Eagle Medium (DMEM), penicillin-streptomycin solution, fetal bovine serum (FBS), trypsin-EDTA solution, and phosphate buffer saline (PBS) were purchased from Gibco (AG, United States). All chemicals were used as received without further purification, and their aqueous solutions were prepared using deionized water.

3.2 Synthesis of 2D Cu-TCPP(Fe) Metal-Organic Frameworks

A mixture of $Cu(NO_3)_2{\cdot}3H_2O$ (4.8 mg, 0.02 mmol), TCPP(Fe) (8.8 mg, 0.01 mmol), CF_3COOH (20 μL, 1.0 M), DMF (1.5 ml), and ethanol (0.5 ml) was added into a small, capped vial, which was then heated to 80°C and kept for 24 h. The resulting dark-brown crystals were washed with ethanol and re-dispersed in ethanol.

The as-prepared Cu-TCPP(Fe) MOFs are hydrophilic and cannot be used for future biological applications. To solve this problem, a "thin-film" approach was used to produce SP-encapsulated Cu-TCPP(Fe) MOFs [Cu-TCPP(Fe)-SP]. Typically, 2 ml of Cu-TCPP(Fe) MOFs in ethanol solution (1 mg/ml) was added into 10 ml of SP in chloroform solution (1 mg/ml) and sonicated for 5 min. The mixture was incubated in a vacuum rotary evaporator at 60°C for 30 min to evaporate the

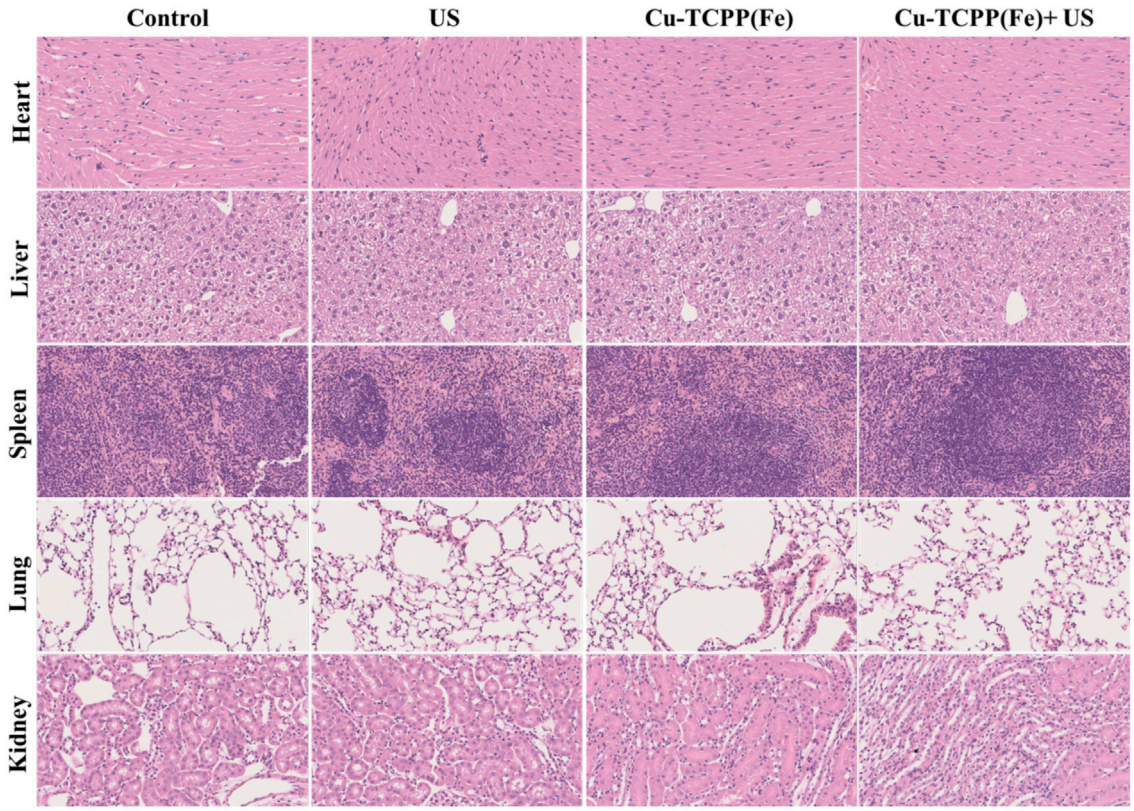

FIGURE 8 | Histopathological examinations of major organs (heart, liver, spleen, lung, and kidney) from mice after different treatments. Scale bar: 50 μm.

solvent. Subsequently, 10 ml of PBS was added into the lipidic film and then sonicated for 10 min.

3.3 Characterization

Transmission electron microscopy (TEM) images and energy-dispersive X-ray spectra (EDS) were acquired using a JEM-2100F transmission electron microscope operated at 200 kV. X-ray diffraction (XRD) was performed on a Rigaku D/MAX-2200 PC XRD system with Cu Kα radiation (λ = 1.54 Å) at 40 kV and 40 mA. Scanning electron microscopy (SEM) images and element mapping were captured by FEI Magellan 400 scanning electron microscope (FEI Company, United States). XPS spectra were recorded by ESCAlab250 (Thermal Scientific). The CLSM images were measured on an FV1000 (Olympus Company, Japan). The optical absorbance spectra were conducted on a Molecular Device SpectraMax M2. The concentrations of copper and iron were measured by using inductively coupled plasma optical emission spectrometry (ICP-OES, OPTIMA 7000DV).

3.4 Cell Culture and Animals

Mouse breast cancer cell 4T1 cells were used in all of these experiments, which were cultured in high glucose DMEM media supplemented with 10% FBS and 1% penicillin-streptomycin. The cells were maintained at 37°C in a humidified incubator with 5% CO_2.

Healthy female Kunming mice (18–22 g, 6–8 weeks) and female BALB/c nude mice (18–22 g, 6–8 weeks) were obtained from Beijing Vital River Laboratory Animal Technology Co., Ltd. and raised at the Laboratory Animal Center at Shanghai Medical College of Fudan University. All animal experiments were conducted in agreement with the guidelines of the Regional Ethics Committee for Animal Experiments, and the care regulations were approved by the Administrative Committee of Laboratory Animals of Fudan University.

3.5 *In vitro* Reactive Oxygen Species Generation by Sonodynamic Therapy

The cells were co-incubated with Cu-TCPP(Fe) (1 ml, 20 μg/ml in DMEM) at 37°C for 4 h. Then, the cells were incubated for another 4 h after being treated by US irradiation (1.0 MHz, 1.5 W/cm^2, 50% duty cycle, 1 min). The cells were washed with PBS three times after staining for 15 min with DCFH-DA (100 μL, 1 μL/9 μL in DMEM), and finally observed by CLSM.

3.6 CLSM Evaluation of the Sonotoxicity of Cu-TCPP(Fe)

The cell processing procedures were similar to those in ROS generation mentioned above; however, the culture medium was replaced with Calcein-AM (100 μL, 20 μM) and PI (100 μL, 20 μM) to stain the live and dead cells, respectively.

3.7 *In vitro* Sonodynamic Therapy Efficacy of Cu-TCPP(Fe) Against Tumor Cells

4T1 cells were cultured and seeded in 96-well plates at a density of 1×10^4 cells per well for 12 h to allow them to stick to the plate. Then, Cu-TCPP(Fe) (20, 10, 5, 2.5, 1.25, and 0.625 μg/ml) was added to the well and co-incubated for another 4 h. Then the cells were treated with US irradiation (1.0 MHz, 1.5 W/cm^2, 50% duty cycle) for 30, 90, and 120 s. CCK-8 (100 μL, $V_{CCK\text{-}8}$: V_{DMEM} = 1: 9) was then used to examine the cell inhibition rate on a microplate reader at the wavelength 450 nm after 90 min.

3.8 Michaelis-Menten Kinetics

TMB (0.8 mg/ml) was applied to monitor the chromogenic reaction (λ = 650 nm) of 20 μg/ml Cu-TCPP(Fe) upon addition of various concentrations of H_2O_2 (40, 20, 10, and 5 mM). The trigger of US (1.0 MHz, 1.5 W/cm^2, 50% duty cycle, 1 min) was applied to verify the enhancement of SDT. Sodium citrate buffer solution (pH = 6.0) was used to prepare the above reagents. The Michaelis-Menten kinetic curve of Cu-TCPP(Fe) was acquired by plotting the respective initial velocities against H_2O_2 concentrations. The Michaelis-Menten constant (K_M) and maximal velocity (V_{max}) were calculated *via* the Lineweaver-Burk plotting.

3.9 Bleaching of MB by Reactive Oxygen Species

MB (200 μL) was used to monitor the chromogenic reaction (λ = 664 nm) of 40 μg/ml Cu-TCPP(Fe) upon addition of 40 mM H_2O_2. Sodium citrate buffer solution (pH = 6.0) was used to bring the final volume to 3 ml. Further, 200 μL MB and 40 mM H_2O_2 were added into 3 ml of sodium citrate buffer solution (pH = 6.0) to observe the bleaching ability of H_2O_2. The trigger of US (1.0 MHz, 1.5 W/cm^2, 50% duty cycle, 1 min) was applied to verify the enhancement of SDT. MB (200 μL) in 3 ml of sodium citrate buffer solution (pH = 6.0) was set as the control. The spectrum of MB in the different groups was acquired at different time points (5, 15, 30, 60, 90, 120, 150, and 180 min).

3.10 *In vivo* Sonodynamic Therapy Efficiency of Cu-TCPP(Fe) Against Tumor Growth

A total of 20 female BALB/c nude mice were subcutaneously injected with 4T1 cells (1×10^6 cells/mouse) to establish the tumor model. When the tumor volume reached 40 mm^3, the mice were divided into 4 groups (n = 5 in each group): 1) control group, 2) US group, 3) Cu-TCPP(Fe) group, and 4) Cu-TCPP(Fe) + US group. The mice in the Cu-TCPP(Fe) + US group and Cu-TCPP(Fe) group were intravenously injected with Cu-TCPP(Fe) (10 mg/kg). The mice in the Cu-TCPP(Fe) + US group and US group were treated with US irradiation (1.0 MHz, 2.3 W/cm^2, 50% duty cycle, 5 min) after injection of Cu-TCPP(Fe) for days 1 and 5. The tumor volume was calculated as follows, $V = (ab^2)/2$, where a and b refer to the largest length and width of the tumor, respectively. The tumor volume was recorded and photographed every 2 d. At the end of the treatment, the tumor was cut and stained by H&E, TUNEL, and Ki-67 for histological analysis.

4 CONCLUSION

A concept of SDT combined with chemical catalysis has been introduced into the field of nanomedicine to effectively inhibit tumor growth by Cu-TCPP(Fe) MOFs with excellent biodegradability and biocompatibility. The porphyrin structure in Cu-TCPP(Fe) is effectively triggered by US, which results in a microenvironment of H_2O_2 and acid within the tumor tissue. This microenvironment is subsequently used in Fe-based chemo-Fenton reactions, which results in increased levels of toxic hydroxyl radicals that induce tumor cell apoptosis and death. This work showed that introducing well-designed nanocatalysts into tumor tissue could trigger a specific sequence of specific TME responses that inhibit tumor growth. Thus, we provided here a promising strategy for tumor therapy that could greatly enhance tumor specificity and reduce side effects on normal tissue.

DATA AVAILABILITY STATEMENT

The original contributions presented in the study are included in the article/**Supplementary Material,** further inquiries can be directed to the corresponding author.

ETHICS STATEMENT

The animal study was reviewed and approved by Administrative Committee of Laboratory Animals of Fudan University.

AUTHOR CONTRIBUTIONS

HZ, YL, and CC conceived the study and participated in the experiment design. HZ and YL performed the experiment. JL provided experimental technical guidance. HZ and YL completed figures construction and manuscript writing. CC checked and revised the manuscript. All authors discussed the results and approved the final version.

FUNDING

This work was supported by the National Nature Science Foundation of China (Grant No. 81901749, 81602262 and 81801701) and the Shanghai Sailing Program (Grant No. 19YF1410000).

SUPPLEMENTARY MATERIAL

The Supplementary Material for this article can be found online at: https://www.frontiersin.org/articles/10.3389/fmats.2022.908789/full#supplementary-material

REFERENCES

Allison, R. R., and Sibata, C. H. (2010). Oncologic Photodynamic Therapy Photosensitizers: a Clinical Review. *Photodiagnosis Photodyn. Ther.* 7 (2), 61–75. doi:10.1016/j.pdpdt.2010.02.001

An, Q., Sun, C., Li, D., Xu, K., Guo, J., and Wang, C. (2013). Peroxidase-like Activity of Fe3O4@carbon Nanoparticles Enhances Ascorbic Acid-Induced Oxidative Stress and Selective Damage to PC-3 Prostate Cancer Cells. *ACS Appl. Mat. Interfaces* 5 (24), 13248–13257. doi:10.1021/am4042367

Burkitt, M. J., and Gilbert, B. C. (1990). Model Studies of the Iron-Catalysed Haber-Weiss Cycle and the Ascorbate-Driven Fenton Reaction. *Free Radic. Res. Commun.* 10 (4-5), 265–280. doi:10.3109/10715769009149895

Carmeliet, P., and Jain, R. K. (2000). Angiogenesis in Cancer and Other Diseases. *Nature* 407 (6801), 249–257. doi:10.1038/35025220

Castano, A. P., Mroz, P., and Hamblin, M. R. (2006). Photodynamic Therapy and Anti-tumour Immunity. *Nat. Rev. Cancer* 6 (7), 535–545. doi:10.1038/nrc1894

Chen, Z., Yin, J.-J., Zhou, Y.-T., Zhang, Y., Song, L., Song, M., et al. (2012). Dual Enzyme-like Activities of Iron Oxide Nanoparticles and Their Implication for Diminishing Cytotoxicity. *ACS Nano* 6 (5), 4001–4012. doi:10.1021/nn300291r

Cheng, L., Liu, J., Gu, X., Gong, H., Shi, X., Liu, T., et al. (2014). PEGylated WS2Nanosheets as a Multifunctional Theranostic Agent for *In Vivo* Dual-Modal CT/Photoacoustic Imaging Guided Photothermal Therapy. *Adv. Mat.* 26 (12), 1886–1893. doi:10.1002/adma.201304497

Chhowalla, M., Shin, H. S., Eda, G., Li, L.-J., Loh, K. P., and Zhang, H. (2013). The Chemistry of Two-Dimensional Layered Transition Metal Dichalcogenide Nanosheets. *Nat. Chem.* 5 (4), 263–275. doi:10.1038/nchem.1589

Chu, K. F., and Dupuy, D. E. (2014). Thermal Ablation of Tumours: Biological Mechanisms and Advances in Therapy. *Nat. Rev. Cancer* 14 (3), 199–208. doi:10.1038/nrc3672

Coussens, L. M., and Werb, Z. (2002). Inflammation and Cancer. *Nature* 420 (6917), 860–867. doi:10.1038/nature01322

DeBerardinis, R. J., and Chandel, N. S. (2016). Fundamentals of Cancer Metabolism. *Sci. Adv.* 2 (5), e1600200. doi:10.1126/sciadv.1600200

Deepagan, V. G., You, D. G., Um, W., Ko, H., Kwon, S., Choi, K. Y., et al. (2016). Long-Circulating Au-TiO2 Nanocomposite as a Sonosensitizer for ROS-Mediated Eradication of Cancer. *Nano Lett.* 16, 6257–6264. doi:10.1021/acs.nanolett.6b02547

Dolmans, D. E. J. G. J., Fukumura, D., and Jain, R. K. (2003). Photodynamic Therapy for Cancer. *Nat. Rev. Cancer* 3 (5), 380–387. doi:10.1038/nrc1071

Firczuk, M., Nowis, D., and Gołąb, J. (2011). PDT-induced Inflammatory and Host Responses. *Photochem. Photobiol. Sci.* 10 (5), 653–663. doi:10.1039/c0pp00308e

Galadari, S., Rahman, A., Pallichankandy, S., and Thayyullathil, F. (2017). Reactive Oxygen Species and Cancer Paradox: To Promote or to Suppress? *Free Radic. Biol. Med.* 104, 144–164. doi:10.1016/j.freeradbiomed.2017.01.004

Gao, L., Zhuang, J., Nie, L., Zhang, J., Zhang, Y., Gu, N., et al. (2007). Intrinsic Peroxidase-like Activity of Ferromagnetic Nanoparticles. *Nat. Nanotech* 2 (9), 577–583. doi:10.1038/nnano.2007.260

Guo, W., Xia, W., Cai, K., Wu, Y., Qiu, B., Liang, Z., et al. (2017). Kinetic-Controlled Formation of Bimetallic Metal-Organic Framework Hybrid Structures. *Small* 13 (41), 2049. doi:10.1002/smll.201702049

Hanahan, D., and Weinberg, R. A. (2011). Hallmarks of Cancer: the Next Generation. *Cell* 144 (5), 646–674. doi:10.1016/j.cell.2011.02.013

Harada, Y., Ogawa, K., Irie, Y., Endo, H., Feril, L. B., Jr., Uemura, T., et al. (2011). Ultrasound Activation of TiO2 in Melanoma Tumors. *J. Control. Release* 149 (2), 190–195. doi:10.1016/j.jconrel.2010.10.012

Hofmans, S., Berghe, T. V., Devisscher, L., Hassannia, B., Lyssens, S., Joossens, J., et al. (2016). Novel Ferroptosis Inhibitors with Improved Potency and ADME Properties. *J. Med. Chem.* 59 (5), 2041–2053. doi:10.1021/acs.jmedchem.5b01641

Hornsveld, M., and Dansen, T. B. (2016). The Hallmarks of Cancer from a Redox Perspective. *Antioxidants Redox Signal.* 25 (6), 300–325. doi:10.1089/ars.2015.6580

Huang, P., Qian, X., Chen, Y., Yu, L., Lin, H., Wang, L., et al. (2017). Metalloporphyrin-Encapsulated Biodegradable Nanosystems for Highly Efficient Magnetic Resonance Imaging-Guided Sonodynamic Cancer Therapy. *J. Am. Chem. Soc.* 139 (3), 1275–1284. doi:10.1021/jacs.6b11846

Huang, Y., Zhao, M., Han, S., Lai, Z., Yang, J., Tan, C., et al. (2017). Growth of Au Nanoparticles on 2D Metalloporphyrinic Metal-Organic Framework Nanosheets Used as Biomimetic Catalysts for Cascade Reactions. *Adv. Mater* 29 (32), 102. doi:10.1002/adma.201700102

Kou, J. Y., Li, Y., Zhong, Z. Y., Jiang, Y. Q., Li, X. S., Han, X. B., et al. (2017). Berberine-sonodynamic Therapy Induces Autophagy and Lipid Unloading in Macrophage. *Cell Death Dis.* 8 (1), e2558. doi:10.1038/cddis.2016.354

Kwon, B., Han, E., Yang, W., Cho, W., Yoo, W., Hwang, J., et al. (2016). Nano-Fenton Reactors as a New Class of Oxidative Stress Amplifying Anticancer Therapeutic Agents. *ACS Appl. Mat. Interfaces* 8 (9), 5887–5897. doi:10.1021/acsami.5b12523

Landry, W. D., and Cotter, T. G. (2014). ROS Signalling, NADPH Oxidases and Cancer. *Biochem. Soc. Trans.* 42 (4), 934–938. doi:10.1042/bst20140060

Li, W.-P., Su, C.-H., Chang, Y.-C., Lin, Y.-J., and Yeh, C.-S. (2016). Ultrasound-Induced Reactive Oxygen Species Mediated Therapy and Imaging Using a Fenton Reaction Activable Polymersome. *ACS Nano* 10 (2), 2017–2027. doi:10.1021/acsnano.5b06175

Liu, J., Wang, H., and Antonietti, M. (2016). Graphitic Carbon Nitride "reloaded": Emerging Applications beyond (Photo)catalysis. *Chem. Soc. Rev.* 45 (8), 2308–2326. doi:10.1039/c5cs00767d

Liu, Y., He, J., Yang, K., Yi, C., Liu, Y., Nie, L., et al. (2015). Folding up of Gold Nanoparticle Strings into Plasmonic Vesicles for Enhanced Photoacoustic Imaging. *Angew. Chem. Int. Ed.* 54 (52), 15809–15812. doi:10.1002/anie.201508616

Liu, Y., Purich, D. L., Wu, C., Wu, Y., Chen, T., Cui, C., et al. (2015). Ionic Functionalization of Hydrophobic Colloidal Nanoparticles to Form Ionic Nanoparticles with Enzymelike Properties. *J. Am. Chem. Soc.* 137 (47), 14952–14958. doi:10.1021/jacs.5b08533

Long, D., Liu, T., Tan, L., Shi, H., Liang, P., Tang, S., et al. (2016). Multisynergistic Platform for Tumor Therapy by Mild Microwave Irradiation-Activated Chemotherapy and Enhanced Ablation. *ACS Nano* 10, 9516–9528. doi:10.1021/acsnano.6b04749

Ma, R., and Sasaki, T. (2015). Two-dimensional Oxide and Hydroxide Nanosheets: Controllable High-Quality Exfoliation, Molecular Assembly, and Exploration of Functionality. *Acc. Chem. Res.* 48 (1), 136–143. doi:10.1021/ar500311w

Makiura, R., Motoyama, S., Umemura, Y., Yamanaka, H., Sakata, O., and Kitagawa, H. (2010). Surface Nano-Architecture of a Metal-Organic Framework. *Nat. Mater* 9 (7), 565–571. doi:10.1038/nmat2769

McEwan, C., Kamila, S., Owen, J., Nesbitt, H., Callan, B., Borden, M., et al. (2016). Combined Sonodynamic and Antimetabolite Therapy for the Improved Treatment of Pancreatic Cancer Using Oxygen Loaded Microbubbles as a Delivery Vehicle. *Biomaterials* 80, 20–32. doi:10.1016/j.biomaterials.2015.11.033

Novoselov, K. S., Geim, A. K., Morozov, S. V., Jiang, D., Zhang, Y., Dubonos, S. V., et al. (2004). Electric Field Effect in Atomically Thin Carbon Films. *Science* 306 (5696), 666–669. doi:10.1126/science.1102896

Pakdel, A., Bando, Y., and Golberg, D. (2014). Nano Boron Nitride Flatland. *Chem. Soc. Rev.* 43 (3), 934–959. doi:10.1039/c3cs60260e

Pelaz, B., Alexiou, C., Alvarez-Puebla, R. A., Alves, F., Andrews, A. M., Ashraf, S., et al. (2017). Diverse Applications of Nanomedicine. *ACS Nano* 11 (3), 2313–2381. doi:10.1021/acsnano.6b06040

Peng, Y., Li, Y., Ban, Y., Jin, H., Jiao, W., Liu, X., et al. (2014). Metal-organic Framework Nanosheets as Building Blocks for Molecular Sieving Membranes. *Science* 346 (6215), 1356–1359. doi:10.1126/science.1254227

Portnow, J., Badie, B., Chen, M., Liu, A., Blanchard, S., and Synold, T. W. (2009). The Neuropharmacokinetics of Temozolomide in Patients with Resectable Brain Tumors: Potential Implications for the Current Approach to Chemoradiation. *Clin. Cancer Res.* 15 (22), 7092–7098. doi:10.1158/1078-0432.ccr-09-1349

Rahim Pouran, S., Abdul Raman, A. A., and Wan Daud, W. M. A. (2014). Review on the Application of Modified Iron Oxides as Heterogeneous Catalysts in Fenton Reactions. *J. Clean. Prod.* 64, 24–35. doi:10.1016/j.jclepro.2013.09.013

Rodenas, T., Luz, I., Prieto, G., Seoane, B., Miro, H., Corma, A., et al. (2015). Metal-organic Framework Nanosheets in Polymer Composite Materials for Gas Separation. *Nat. Mater* 14 (1), 48–55. doi:10.1038/nmat4113

Satoh, A. Y., Trosko, J. E., and Masten, S. J. (2007). Methylene Blue Dye Test for Rapid Qualitative Detection of Hydroxyl Radicals Formed in a Fenton's

Reaction Aqueous Solution. *Environ. Sci. Technol.* 41 (8), 2881–2887. doi:10.1021/es0617800

Siegel, R. L., Miller, K. D., Fuchs, H. E., and Jemal, A. (2021). Cancer Statistics, 2021. *CA A Cancer J. Clin.* 71 (1), 7–33. doi:10.3322/caac.21654

Simon-Yarza, T., Giménez-Marqués, M., Mrimi, R., Mielcarek, A., Gref, R., Horcajada, P., et al. (2017). A Smart Metal-Organic Framework Nanomaterial for Lung Targeting. *Angew. Chem. Int. Ed.* 56 (49), 15565–15569. doi:10.1002/anie.201707346

Strickland, K., Miner, E., Jia, Q., Tylus, U., Ramaswamy, N., Liang, W., et al. (2015). Highly Active Oxygen Reduction Non-platinum Group Metal Electrocatalyst without Direct Metal-Nitrogen Coordination. *Nat. Commun.* 6, 7343. doi:10.1038/ncomms8343

Su, L., Feng, J., Zhou, X., Ren, C., Li, H., and Chen, X. (2012). Colorimetric Detection of Urine Glucose Based ZnFe2O4 Magnetic Nanoparticles. *Anal. Chem.* 84 (13), 5753–5758. doi:10.1021/ac300939z

Tan, C., and Zhang, H. (2015). Two-dimensional Transition Metal Dichalcogenide Nanosheet-Based Composites. *Chem. Soc. Rev.* 44 (9), 2713–2731. doi:10.1039/c4cs00182f

Trachootham, D., Alexandre, J., and Huang, P. (2009). Targeting Cancer Cells by ROS-Mediated Mechanisms: a Radical Therapeutic Approach? *Nat. Rev. Drug Discov.* 8 (7), 579–591. doi:10.1038/nrd2803

Wang, Q., Hu, B., Hu, X., Kim, H., Squatrito, M., Scarpace, L., et al. (2017). Tumor Evolution of Glioma-Intrinsic Gene Expression Subtypes Associates with Immunological Changes in the Microenvironment. *Cancer Cell* 32 (1), 42–56. doi:10.1016/j.ccell.2017.06.003

Xu, G., Yamada, T., Otsubo, K., Sakaida, S., and Kitagawa, H. (2012). Facile "modular Assembly" for Fast Construction of a Highly Oriented Crystalline MOF Nanofilm. *J. Am. Chem. Soc.* 134 (40), 16524–16527. doi:10.1021/ja307953m

Zhang, C., Zhao, K., Bu, W., Ni, D., Liu, Y., Feng, J., et al. (2015). Marriage of Scintillator and Semiconductor for Synchronous Radiotherapy and Deep Photodynamic Therapy with Diminished Oxygen Dependence. *Angew. Chem. Int. Ed.* 54 (6), 1770–1774. doi:10.1002/anie.201408472

Zhang, C., Bu, W., Ni, D., Zhang, S., Li, Q., Yao, Z., et al. (2016). Synthesis of Iron Nanometallic Glasses and Their Application in Cancer Therapy by a Localized Fenton Reaction. *Angew. Chem. Int. Ed.* 55 (6), 2101–2106. doi:10.1002/anie.201510031

Zou, Z., Chang, H., Li, H., and Wang, S. (2017). Induction of Reactive Oxygen Species: an Emerging Approach for Cancer Therapy. *Apoptosis* 22 (11), 1321–1335. doi:10.1007/s10495-017-1424-9

Conflict of Interest: The authors declare that the research was conducted in the absence of any commercial or financial relationships that could be construed as a potential conflict of interest.

Publisher's Note: All claims expressed in this article are solely those of the authors and do not necessarily represent those of their affiliated organizations, or those of the publisher, the editors and the reviewers. Any product that may be evaluated in this article, or claim that may be made by its manufacturer, is not guaranteed or endorsed by the publisher.